nature geoscience

ARTICLES

https://doi.org/10.1038/s41561-018-0271-9

Twenty-first century glacier slowdown driven by mass loss in High Mountain Asia

Amaury Dehecq[1,2,3*], Noel Gourmelen[3,4], Alex S. Gardner[1], Fanny Brun[5,6], Daniel Goldberg[3], Peter W. Nienow[3], Etienne Berthier[6], Christian Vincent[5], Patrick Wagnon[5] and Emmanuel Trouvé[2]

Glaciers in High Mountain Asia have experienced heterogeneous rates of loss since the 1970s. Yet, the associated changes in ice flow that lead to mass redistribution and modify the glacier sensitivity to climate are poorly constrained. Here we present observations of changes in ice flow for all glaciers in High Mountain Asia over the period 2000–2017, based on one million pairs of optical satellite images. Trend analysis reveals that in 9 of the 11 surveyed regions, glaciers show sustained slowdown concomitant with ice thinning. In contrast, the stable or thickening glaciers of the Karakoram and West Kunlun regions experience slightly accelerated glacier flow. Up to 94% of the variability in velocity change between regions can be explained by changes in gravitational driving stress, which in turn is largely controlled by changes in ice thickness. We conclude that, despite the complexities of individual glacier behaviour, decadal and regional changes in ice flow are largely insensitive to changes in conditions at the bed of the glacier and can be well estimated from ice thickness change and slope alone.

Glaciers are thinning world-wide, at an increasing rate since the turn of the twenty-first century[1], with a mean mass balance of −0.42 m w.e. yr^{-1} (meter water-equivalent per year)[2]. Glaciers on the Tibetan Plateau and surrounding ranges (Fig. 1), referred to as High Mountain Asia (HMA), are no exception despite regionally contrasted evolution: some regions are experiencing close to global mean rates of mass loss—for example, Spiti Lahaul (−0.37 ± 0.09 m w.e. yr^{-1}), West Nepal (−0.34 ± 0.09 m w.e. yr^{-1}) or Nyainqêntanglha (−0.62 ± 0.23 m w.e. yr^{-1})[3]—whereas glaciers north-west of the Tibetan Plateau (West Kunlun Shan, Karakoram, East Pamir) are near equilibrium or slightly gaining mass[3–5]. This contrasted pattern has persisted since the 1970s[6].

In response to these mass changes, glacier flow is expected to change, thereby affecting ice fluxes, hypsometry (ice area–altitude distribution) and glacier mass balance. However, the link between these different components and, in particular, the flow response of glaciers to mass change are poorly understood at regional scales[7]. Dynamic mass redistribution is particularly critical in regional glacier models used to estimate glacier contributions to sea-level change[8–10] and water resources[11], but is generally represented by empirical scalings, which lack a physical representation of glacier flow[12]. A few studies have attempted to model ice flow at regional scales, taking into account ice deformation[12,13] or basal sliding[14,15], but the justification of model choice is generally undermined by the lack of velocity observations[16].

Field measurements demonstrate that ice flow of land-terminating glaciers fluctuates with mass changes at decadal scales[17,18]. Another paper[7] analysed ice velocity changes over recent decades using single satellite image pairs from six glacierized regions in the world. They conclude that ice flow slowed in regions with negative mass balance but found no clear relation between mass balance and velocity change. The slowdown of several land-terminating glaciers has been observed locally in HMA, concomitant with negative mass balance[19–22], but no observation of velocity changes exists at regional scales.

In this study we measure regional changes in the flow of HMA glaciers using systematic feature-tracking of repeat satellite images collected between 2000 and 2017. We discuss regional differences in velocity trends with regards to known ice thickness changes over a similar period. Finally, we estimate the contribution of changes in gravitational driving stress to the observed changes in surface velocity and discuss the best representation of ice flow in models of glacier evolution.

Interannual changes in glacier velocities

We derive glacier surface velocities by applying feature-tracking to 907,142 panchromatic Landsat-7 image pairs (15 m resolution) separated by less than 545 days using JPL auto-RIFT software[23] (Methods). We generate a mean velocity field for 94% of all glaciers in HMA from an error-weighted average of all velocity fields over the period 1999–2017 at 240 m resolution. Annual velocities are obtained similarly at yearly intervals for the period 2000–2017 (insufficient data was available for 1999) with glacier coverage ranging from 83 to 89% (Supplementary Fig. 1). Image pairs span one year on average, centred around June, with little interannual variability (Supplementary Figs. 2 and 3). Consequently, our results are relatively insensitive to seasonal fluctuations in ice flow. The velocity uncertainty, estimated over ice-free terrain, varies with the number of available image pairs and changes in radiometric quality[24]. The median uncertainty of the annual velocity fields is around 2 m yr^{-1}, with a minimum (~0.8 m yr^{-1}) for the central and eastern Himalaya and a maximum (3 m yr^{-1}) for the Tibetan Plateau (Supplementary Fig. 4). Examples of velocity maps are shown on Supplementary Fig. 5a,c,e.

To extract regional velocity trends, we conduct our analysis on glacier areas with surface velocities that substantially exceed the estimated uncertainty. We select pixels with a mean velocity greater than 5 m yr^{-1} over glaciers larger than 5 km^2 (areas from ref. [25]). Accumulation zones have larger measurement uncertainties due to

[1]Jet Propulsion Laboratory, California Institute of Technology, Pasadena, CA, USA. [2]Université Savoie Mont Blanc, LISTIC, Annecy, France. [3]School of GeoSciences, University of Edinburgh, Edinburgh, UK. [4]IPGS UMR 7516, Université de Strasbourg, CNRS, Strasbourg, France. [5]Université Grenoble Alpes, CNRS, IRD, Grenoble INP, IGE, Grenoble, France. [6]LEGOS, Université de Toulouse, CNES, CNRS, IRD, UPS, Toulouse, France.
*e-mail: amaury.dehecq@jpl.nasa.gov

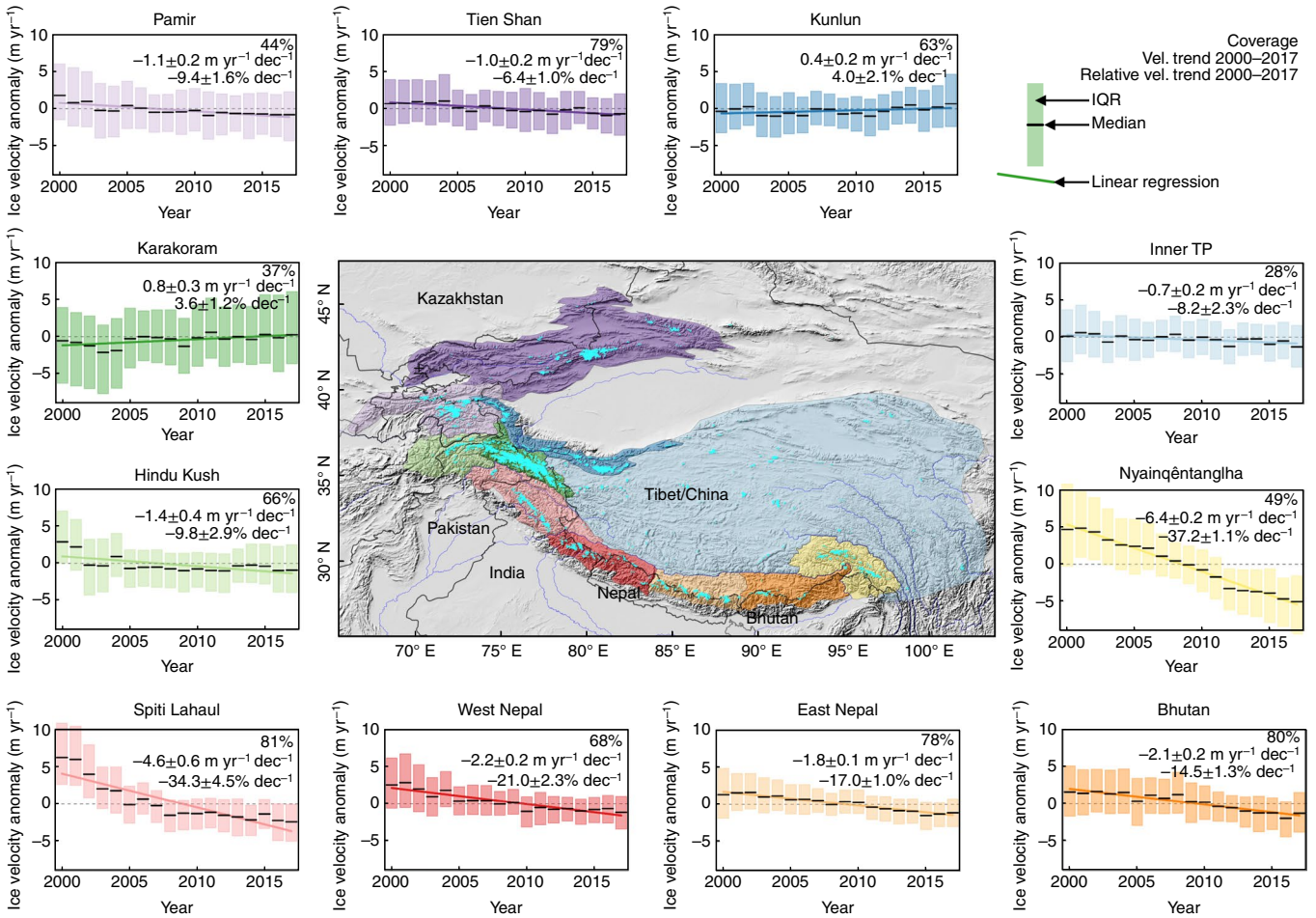

Fig. 1 | Annual glacier velocity anomalies for High Mountain Asia (2000–2017). The centre map shows the study area and 11 subregions with glaciers highlighted in cyan. Each inset shows a time series of the annual velocity anomaly (change along flow direction relative to the mean velocity) for each subregion. Black lines represent the median anomaly, colour bars the interquartile range and coloured lines the linear trend over 2000–2017. Coverage of observations common to all years (top), velocity trend (middle) and velocity trend relative to the mean velocity (bottom), with 68% confidence interval, are reported in each inset. Dec, decade.

low image contrast, and have experienced little elevation change[3]. For this reason, we restrict our analysis to the lower half of each glacier, which approximately represents the ablation zone. Glaciers known to experience surges[26] (surge-type) are included in the general analysis, but their regional response is also quantified and discussed separately. Our observations are uniformly distributed across altitude in the ablation zone and glacier size (above 5 km^2), and are therefore representative of the diversity of glaciers in HMA (Supplementary Section 1).

To characterize regional changes in ice flow, we examine anomalies in annual velocity for each region. We define the velocity anomaly as the vector difference between the annual velocity and the mean velocity, projected to the orientation of the mean velocity (Methods). This scalar variable is positive if the ice flow accelerated along a flow line and negative if it slowed down. This approach ensures that the uncertainty in velocity change is symmetrically centred on zero (Supplementary Fig. 8) as opposed to simply differencing the velocity magnitude (Supplementary Fig. 9). We calculate, for each year and 11 subregions in HMA, the median anomaly over pixels with observations in all years, and compute a linear trend over the period 2000–2017 (Methods).

The results (Fig. 1) show that the largest velocity changes (slowdown) occur for glaciers in Nyainqêntanglha ($-37.2\pm1.1\%$ decade^{-1}) and Spiti Lahaul ($-34.3\pm4.5\%$ decade^{-1}). Smaller but significant slowdowns are observed along the Himalayan range, with decreasing amplitude towards the East: West Nepal ($-21.0\pm2.3\%$ decade^{-1}), East Nepal ($-17.0\pm1.0\%$ decade^{-1}) and Bhutan ($-14.5\pm1.3\%$ decade^{-1}). Contrasted trends are observed in the north-western regions, with negative trends in the Hindu Kush ($-9.8\pm2.9\%$ decade^{-1}), Pamir ($-9.4\pm1.6\%$ decade^{-1}) and Tien Shan ($-6.4\pm1.0\%$ decade^{-1}), whereas a small but significant speed-up is observed for the Karakoram ($3.6\pm1.2\%$ decade^{-1}) and West Kunlun ($4.0\pm2.1\%$ decade^{-1}). Finally, the inner Tibetan Plateau shows a negative trend ($-8.2\pm2.3\%$ decade^{-1}). Very few observations of glacier velocity changes exist in HMA for validation, but our results show good agreement with both field[20] and remote sensing[22] observations (Supplementary Section 2).

Our results reveal that changes in velocity are not always monotonic over the study period. Most regions in the north-west (Pamir, Hindu Kush, Spiti Lahaul and West Nepal) experienced a pronounced slowdown until 2005–2008, with more stable conditions since. In contrast, East Nepal and Nyainqêntanglha experienced a steady and continuous slowdown, whereas Bhutan experienced a slight increase in its rate of slowdown after 2008. These patterns are consistent with glacier mass balance and elevation change trends[27]. It is noteworthy that the strongest trends are generally observed over 2003–2008, coinciding with the period of observations of the satellite altimeter ICESat, suggesting that

elevation changes derived from ICESat are potentially more negative than the longer term trend[3].

Our analysis focuses on results determined from a single sensor (Landsat 7) due to biases that we identified between velocities derived from different Landsat missions (Supplementary Section 3). However, trends estimated between 1988 and 2017 with over two million image pairs from the Landsat missions 5–8, and accounting for inter-mission biases, lead to similar results despite larger uncertainties, except for a break in trend observed for Spiti Lahaul and Nyainqêntanglha around year 2000 (Supplementary Fig. 12). This is consistent with stable conditions observed in Spiti Lahaul for the 1990s[28,29].

Link between regional velocity trends and mass balance

Trends in velocity anomalies are calculated for each 240-m pixel over the period 2000–2016 (Methods) to match the observation period of glacier thickness change[3]. Examples of velocity trend maps are shown on Supplementary Fig. 5. The results are presented as a median velocity trend on a 1°×1° grid (Fig. 2a) next to rates of elevation change (Fig. 2b). The similarity between patterns of velocity and thickness change, the latter being largely driven by differences in mass balance sensitivity to temperature[30] and different climatic conditions[31], suggests that the spatial variability in velocity change is also influenced by regional differences in climate and glacier sensitivity to temperature. Slowdown along the Himalayan range, Nyainqêntanglha or Tien Shan, for example, is associated with ice thinning, whereas stable or increased glacier flow is observed along with stable to positive mass balance around the Tibetan Plateau and Tarim basin (the so-called 'Karakoram anomaly'). However, some trends differ, notably the speed-up observed in western Tien Shan in a region of negative mass balance and areas of slowdown in West Kunlun, a region of positive mass balance. The regional velocity trend derived for these regions is particularly sensitive to the selected area and the discrepancies are probably related to incomplete spatial sampling of the velocities, or to the large flow variability of these regions, caused by surge activity for instance. At regional scales, changes in glacier velocity and glacier-wide mass balance are strongly correlated (Fig. 3a, $R^2=0.76$). This relationship implies that surface velocity change can be used as a proxy for regional glacier evolution in areas and during periods where regional glacier mass balance is not available. This possibility is especially interesting since surface velocity is more easily obtained from remote-sensing than elevation measurements.

Ice dynamical response to thickness change

Ice flow is primarily controlled by the driving stress (horizontal component of the ice weight per unit area), which causes ice deformation (creep) and sliding over or deformation of the bed[32]. Observations (ref. [32] section 8.3) have shown that surface velocity due to creep is a function of the glacier thickness and driving stress. Basal velocity on the other hand is poorly constrained due to complexities at the glacier bed (bed roughness, type of bed) and is often represented by a power-law of the driving stress[33,34]. In these theoretical frameworks, the surface velocity U_s observed by remote sensing, the sum of both contributions, is therefore expected to respond instantaneously to a change in driving stress. Field-based studies on the other hand have observed a relationship between mass balance and ice flow changes with a lag of one to three years, suggested to be the time taken to diffusively propagate a change in mass load[17,18].

Here, we assume that surface velocity can be represented by the relationship (see Methods and Supplementary Section 5):

$$U_s = C\tau^m \quad (1)$$

where C and m are unknown parameters and τ is the driving stress. By allowing for differing values of the exponent m, this relationship encompasses flow due to both ice deformation and basal sliding (see Methods). C is likely to vary spatially, and depends on local parameters such as ice rheology, valley shape and bed roughness, whereas m is related to the processes leading to ice flow. We further assume that neither C nor m vary significantly with time over the study period. In these conditions, a change in velocity δU_s is related to a change in driving stress $\delta\tau$ by

$$\log\left(1+\frac{\delta U_s}{U_s}\right) = m\,\log\left(1+\frac{\delta\tau}{\tau}\right) \quad (2)$$

with m to be determined.

To test these hypotheses, we calculate the change in driving stress, associated with the changes in thickness observed by ref. [3], along glacier centre flow lines for the period 2000–2016. Measurements of ice thickness are required to calculate the exact driving stress (equation (10)), but are unavailable across the whole HMA. We therefore use modelled thickness estimates that have uncertainties of ~25%[35,36]. We use the ice surface elevation from the Shuttle Radar Topography Mission (SRTM) version 3[37] for year 2000 and from an application of elevation change rates over the period 2000–2016[3] for year 2016. Ice thickness and elevation are extracted along glacier centre flow lines at 50-m spacing to calculate a relative change in thickness and driving stress between 2000 and 2016. We perform the calculations for 2,894 glaciers larger than 5 km^2 and calculate a median driving stress change in ablation zones for each subregion, which we then compare with median velocity changes calculated over the same points. To identify a possible lag of a few years between driving stress and velocity change, we compare the driving stress change over 2000–2016 with the observed velocity anomaly trends for three periods: 2000–2016 (instantaneous response), 2001–2017 (1 year lag) and 2003–2017 (~3 year lag). Larger lags are not considered due to the lack of observations after 2017, which increases uncertainties in later trends.

Our results show that changes in driving stress can explain up to 94% of the inter-regional variability in the observed velocity change with a 3-year lag (Fig. 3b, $R^2=0.94$). We also observe that the strength of the correlation is improved with a 3-year lag as opposed to a 1-year lag ($R^2=0.85$) or no lag ($R^2=0.75$) (Supplementary Fig. 17). Possible explanations for this lag are the diffusive propagation of the thickness change, or adjustment of the bed and subglacial environment to thickness change, that cause a delay in the velocity response[17]. A least-squares regression indicates that the velocity change is best represented by the power $m=4.0$ (68% confidence interval [3.4–4.7]) of the change in driving stress.

The change in driving stress is a combination of change in thickness and slope (equation (10)). Glacier thinning is generally more pronounced at lower elevations[3], causing an increase in slope, that in turn counteracts the reduction in driving stress caused by the thinning. Our results show that the change in driving stress obtained by taking into account the change in thickness and slope is reduced by 15% as compared to accounting for thickness alone (Supplementary Fig. 18). The change in slope indeed offsets the impact of the thinning at lower elevations, but thickness change remains the main contributor to the change in driving stress.

Many glaciers in HMA, mostly located in the Karakoram, Pamir, West Kunlun and Tien Shan[26], experience surges—that is, velocity fluctuations primarily driven by internal glacier instabilities as opposed to climate (ref. [32] chap. 12). It is important to determine whether such glaciers must be considered separately for future projections. Surge-type glaciers are identified using previous studies[5,26,38,39] and from the data generated as part of this study (Supplementary Section 4). Our results do not differ significantly when surge-type glaciers are excluded, in particular the annual velocity anomaly time series (Supplementary Fig. 14) or the velocity

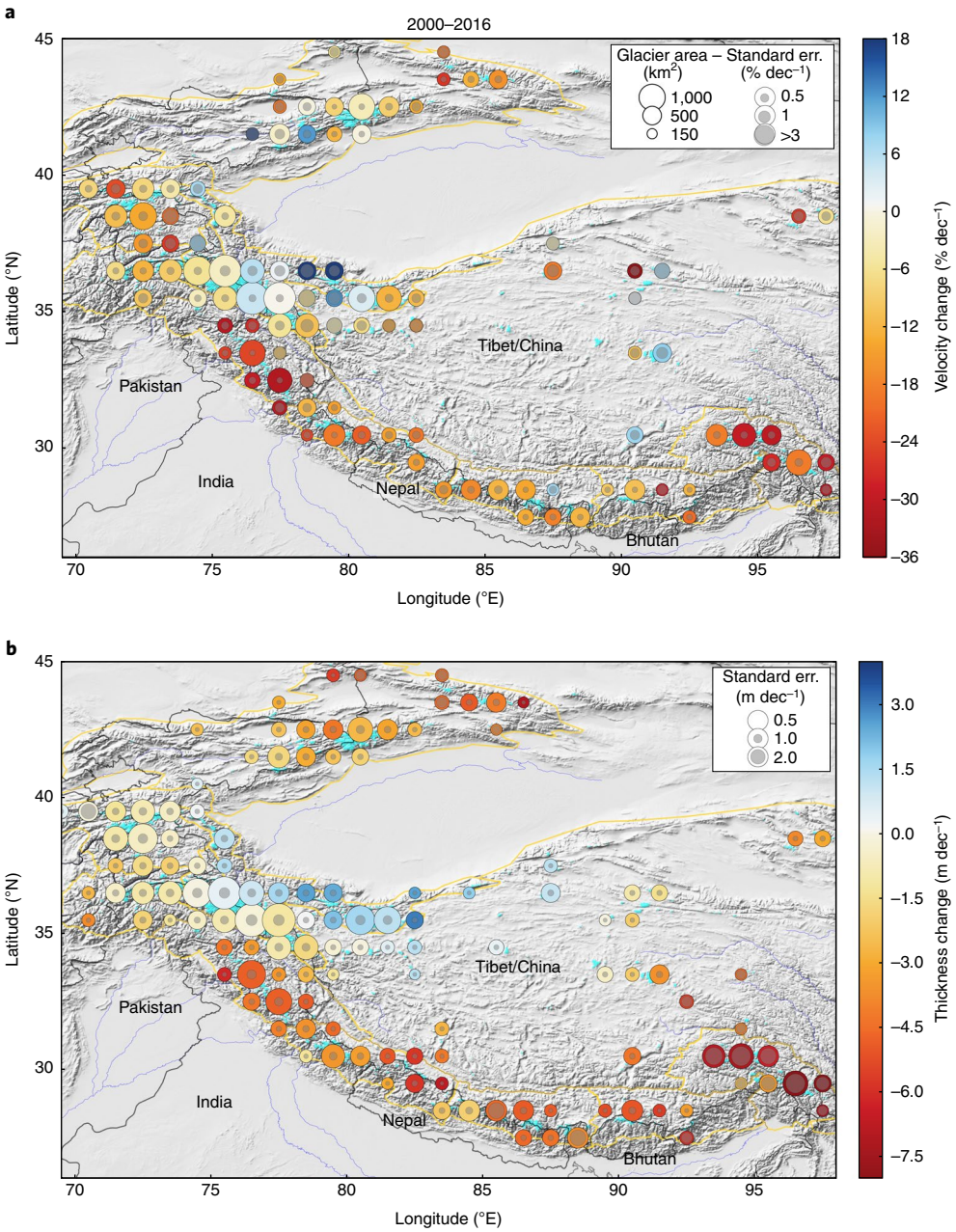

Fig. 2 | Glacier velocity and thickness trends for High Mountain Asia (2000–2016). a, Map of median velocity trend on a 1°×1° grid. Dot colour represents the median velocity trend and its size represents the total glacierized area. The standard error is represented by a grey dot whose area is proportional to the uncertainty and the size of the original dot. **b**, Same figure for thickness change, adapted from ref. [3]. Outlines of the subregions of Fig. 2 are represented in yellow and glaciers in cyan.

trend map (Supplementary Fig. 15). The power-law relationship between driving stress and velocity change remains unaltered with surge-type glaciers both included (Fig. 3b, black-edge dots) or excluded (Fig. 3b, grey-edge dots, $R^2=0.95$). The fact that surge-type glaciers have a similar regional average response as other glaciers is probably due to the heterogeneity in surge characteristics (onset, duration) within a region[39], which tends to average out over sufficiently large spatial and temporal scales. As a consequence, surging behaviour does not need to be considered to correctly estimate the average flow response of glaciers at regional scales.

Implications for regional glacier models

Our findings have important consequences for understanding, and thus modelling, glacier response to environmental forcing. Our results show that the main driver of decadal and regional velocity change is the change in driving stress (Fig. 3b), primarily attributable to changes in thickness (Supplementary Fig. 18). This is supported by ref. [40], which showed that changes in basal and surface velocity of the Argentière glacier, French Alps, are driven by thickness change. This implies that ice flow response to external forcing over decadal timescales can be estimated from the glacier's slope and thickness alone, which are pre-requisites for any glacier flow model. More complex factors such as basal conditions, ice rheology or lateral drag associated with thinning or changing melt regimes, and largely unknown at regional scales, play only a minor role on decadal flow variability and for the range of change in driving stress observed here. It is important to note, however, that driving stress alone does not explain the large inter-glacier variability in our

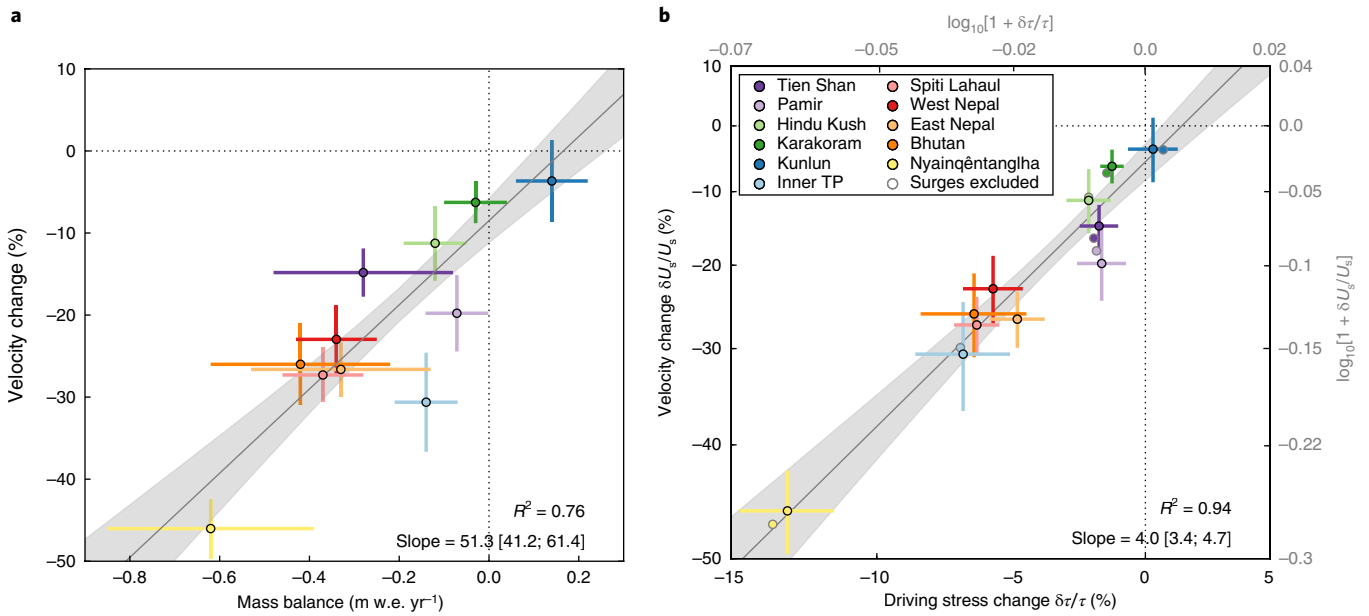

Fig. 3 | Observed velocity change versus mass balance and driving stress change for 11 subregions of HMA. a, Mass balances taken from ref. [3]. **b**, Velocity and driving stress change are median values for glacier centre flowlines. Panel **b** uses logarithmic scales following equation (2). The results presented here are obtained with a lag of three years between velocity and driving stress changes. Coloured dots with black edges include all glaciers, grey edges exclude surge-type glaciers. A linear regression is displayed in grey with coefficient of determination (R^2) and slope provided in the bottom right corner. All error bars represent the 68% confidence interval.

observations (Supplementary Fig. 19). A possible explanation is the uncertainty in individual glacier thicknesses used to calculate the driving stress[36]. Another possible explanation is that changes in subglacial water pressure associated with inputs of surface meltwater, known to play a significant role in driving seasonal fluctuations in surface velocity[40,41], have a larger contribution at the glacier scale, as opposed to the regional scale.

Another uncertainty in glacier modelling is the fraction of basal sliding, known to be important in temperate and polythermal valley glaciers[40,42,43]. A change in driving stress will impact both basal sliding and ice deformation. Our results suggest that surface velocity evolves with the power $m = 4$ of the driving stress. This is consistent with sliding theories incorporating cavitation (ice-bed decoupling in the lee of obstacles when the subglacial pressure is high)[44] leading to an exponent m larger than 3 (see Methods). Furthermore, because changes in thickness and driving stress are very strongly correlated (Supplementary Fig. 18), creep velocity is a function of the fourth power of the driving stress, also compatible with our results (see Methods). This implies that both contributions evolve similarly with the driving stress and their relative contribution remain the same even as driving stress varies. It follows that we cannot separate the contribution of changes in basal sliding and creep velocity to the surface velocity change. More importantly, it also means that surface glacier velocity change can be modelled and parametrized without a priori knowledge or assumptions regarding the fractional contribution of basal sliding. It must be noted, however. that the value retrieved for m is strongly conditioned by the uncertainty in current thickness estimates. An error in the exponent m would lead to an error in ice transport to lower elevations and ice melt (an underestimation of m would lead to an overestimate of mass transport and melt in a thinning scenario, see Supplementary Section 6), with large implications for future estimates of glacier mass changes. However, the complex relationship between ice flow, ice redistribution and mass balance makes it difficult to estimate the impact on the final mass budget. We therefore encourage studies combining observations of decadal glacier flow changes and glacier models to better constrain and reduce uncertainties in glacier dynamics.

In this study, we documented the evolution of surface velocities in the ablation zone of glaciers larger than 5 km² in HMA between 2000–2017, providing an unprecedented and detailed picture of glacier flow response to recent climate change. Our results reveal regionally-heterogeneous trends in surface velocity that parallel changes in ice thickness. Regions of rapid thinning show the largest rates of slowdown (Nyainqêntanglha, Spiti Lahaul), whereas regions near balance or gaining mass have experienced a slight speedup (Karakoram, West Kunlun). The strong relationship between regional glacier mass balance and velocity changes reveals a quasi-instantaneous response of ice flow to climate forcing and suggests that surface velocity can be used as a proxy for glacier state at decadal scales. Analysis along glacier flow lines shows that, at regional scales, 94% of the observed velocity changes can be explained by changes in driving stress, the latter being primarily controlled by changes in ice thickness. Our results suggest that changes in glacier flow in response to mass changes can be estimated in regional glacier models from ice thickness and slope alone, despite poorly constrained basal conditions and rates of basal sliding. These conclusions emphasize the important role played by ice dynamics in glacier response to environmental forcing and will lead to improved modelling of climate–glacier feedbacks and estimates of glacier contributions to hydrology and sea-level change.

Online content

Any methods, additional references, Nature Research reporting summaries, source data, statements of data availability and associated accession codes are available at https://doi.org/10.1038/s41561-018-0271-9.

Received: 11 May 2018; Accepted: 8 November 2018;
Published online: 10 December 2018

References

1. Zemp, M. et al. Historically unprecedented global glacier decline in the early 21st century. *J. Glaciol.* **61**, 745–762 (2015).

2. Gardner, A. S. et al. A reconciled estimate of glacier contributions to sea level rise: 2003 to 2009. *Science* **340**, 852–857 (2013).
3. Brun, F., Berthier, E., Wagnon, P., Kääb, A. & Treichler, D. A spatially resolved estimate of High Mountain Asia glacier mass balances from 2000 to 2016. *Nat. Geosci.* **10**, 668–673 (2017).
4. Kääb, A., Treichler, D., Nuth, C. & Berthier, E. Brief communication: contending estimates of 2003–2008 glacier mass balance over the Pamir–Karakoram–Himalaya. *Cryosphere* **9**, 557–564 (2015).
5. Gardelle, J., Berthier, E., Arnaud, Y. & Kääb, A. Region-wide glacier mass balances over the Pamir–Karakoram–Himalaya during 1999–2011. *Cryosphere* **7**, 1263–1286 (2013).
6. Zhou, Y., Li, Z., Li, J., Zhao, R. & Ding, X. Glacier mass balance in the Qinghai–Tibet Plateau and its surroundings from the mid-1970s to 2000 based on Hexagon KH-9 and SRTM DEMs. *Remote Sens. Environ.* **210**, 96–112 (2018).
7. Heid, T. & Kääb, A. Repeat optical satellite images reveal widespread and long term decrease in land-terminating glacier speeds. *Cryosphere* **6**, 467–478 (2012).
8. Radić, V. et al. Regional and global projections of twenty-first century glacier mass changes in response to climate scenarios from global climate models. *Clim. Dyn.* **42**, 37–58 (2014).
9. Marzeion, B., Jarosch, A. H. & Hofer, M. Past and future sea-level change from the surface mass balance of glaciers. *Cryosphere* **6**, 1295–1322 (2012).
10. Huss, M. & Hock, R. A new model for global glacier change and sea-level rise. *Front. Earth Sci.* **3**, 54 (2015).
11. Huss, M. & Hock, R. Global-scale hydrological response to future glacier mass loss. *Nat. Clim. Change* **8**, 135–140 (2018).
12. Clarke, G. K. C., Jarosch, A. H., Anslow, F. S., Radić, V. & Menounos, B. Projected deglaciation of western Canada in the twenty-first century. *Nat. Geosci.* **8**, 372–377 (2015).
13. Kraaijenbrink, P. D. A., Bierkens, M. F. P., Lutz, A. F. & Immerzeel, W. W. Impact of a global temperature rise of 1.5 degrees Celsius on Asia's glaciers. *Nature* **549**, 257–260 (2017).
14. Immerzeel, W. W., Beek, L. P. Hv, Konz, M., Shrestha, A. B. & Bierkens, M. F. P. Hydrological response to climate change in a glacierized catchment in the Himalayas. *Clim. Change* **110**, 721–736 (2012).
15. Shea, J. M., Immerzeel, W. W., Wagnon, P., Vincent, C. & Bajracharya, S. Modelling glacier change in the Everest region, Nepal Himalaya. *Cryosphere* **9**, 1105–1128 (2015).
16. Azam, M. F. et al. Review of the status and mass changes of Himalayan–Karakoram glaciers. *J. Glaciol.* **64**, 61–74 (2018).
17. Span, N. & Kuhn, M. Simulating annual glacier flow with a linear reservoir model. *J. Geophys. Res.* **108**, 4313 (2003).
18. Vincent, C., Soruco, A., Six, D. & Le Meur, E. Glacier thickening and decay analysis from 50 years of glaciological observations performed on Glacier d'Argentière, Mont Blanc area, France. *Ann. Glaciol.* **50**, 73–79 (2009).
19. Quincey, D. J., Luckman, A. & Benn, D. Quantification of Everest region glacier velocities between 1992 and 2002, using satellite radar interferometry and feature tracking. *J. Glaciol.* **55**, 596–606 (2009).
20. Azam, M. F. et al. From balance to imbalance: a shift in the dynamic behaviour of Chhota Shigri Glacier, western Himalaya, India. *J. Glaciol.* **58**, 315–324 (2012).
21. Sugiyama, S., Fukui, K., Fujita, K., Tone, K. & Yamaguchi, S. Changes in ice thickness and flow velocity of Yala Glacier, Langtang Himal, Nepal, from 1982 to 2009. *Ann. Glaciol.* **54**, 157–162 (2013).
22. Neckel, N., Loibl, D. & Rankl, M. Recent slowdown and thinning of debris-covered glaciers in south-eastern Tibet. *Earth Planet. Sci. Lett.* **464**, 95–102 (2017).
23. Gardner, A. S. et al. Increased West Antarctic and unchanged East Antarctic ice discharge over the last 7 years. *Cryosphere* **12**, 521–547 (2018).
24. Dehecq, A., Gourmelen, N. & Trouve, E. Deriving large-scale glacier velocities from a complete satellite archive: application to the Pamir–Karakoram–Himalaya. *Remote Sens. Environ.* **162**, 55–66 (2015).
25. Pfeffer, W. T. et al. The randolph glacier inventory: a globally complete inventory of glaciers. *J. Glaciol.* **60**, 537 (2014).
26. Sevestre, H. & Benn, D. I. Climatic and geometric controls on the global distribution of surge-type glaciers: implications for a unifying model of surging. *J. Glaciol.* **61**, 646–662 (2015).
27. Wang, Q., Yi, S. & Sun, W. Consistent interannual changes in glacier mass balance and their relationship with climate variation on the periphery of the Tibetan Plateau. *Geophys. J. Int.* **214**, 573–582 (2018).
28. Vincent, C. et al. Balanced conditions or slight mass gain of glaciers in the Lahaul and Spiti region (northern India, Himalaya) during the nineties preceded recent mass loss. *Cryosphere* **7**, 569–582 (2013).
29. Mukherjee, K., Bhattacharya, A., Pieczonka, T., Ghosh, S. & Bolch, T. Glacier mass budget and climate reanalysis data indicate a climatic shift around 2000 in Lahaul–Spiti, western Himalaya. *Clim. Change* **148**, 219–233 (2018).
30. Sakai, A. & Fujita, K. Contrasting glacier responses to recent climate change in high-mountain Asia. *Sci. Rep.* **7**, 13717 (2017).
31. Forsythe, N., Fowler, H. J., Li, X.-F., Blenkinsop, S. & Pritchard, D. Karakoram temperature and glacial melt driven by regional atmospheric circulation variability. *Nat. Clim. Change* **7**, 664–670 (2017).
32. Cuffey, K. M. & Paterson, W. S. B. *The Physics of Glaciers* 4th edn (Elsevier, Burlington, 2010).
33. Weertman, J. On the sliding of glaciers. *J. Glaciol.* **3**, 33–38 (1957).
34. Bindschadler, R. The importance of pressurized subglacial water in separation and sliding at the glacier bed. *J. Glaciol.* **29**, 3–19 (1983).
35. Huss, M. & Farinotti, D. Distributed ice thickness and volume of all glaciers around the globe. *J. Geophys. Res.* **117**, F04010 (2012).
36. Farinotti, D. et al. How accurate are estimates of glacier ice thickness? Results from ITMIX, the Ice Thickness Models Intercomparison eXperiment. *Cryosphere* **11**, 949–970 (2017).
37. Farr, T. G. et al. The shuttle radar topography mission. *Rev. Geophys.* **45**, RG2004 (2007).
38. Rankl, M., Kienholz, C. & Braun, M. Glacier changes in the Karakoram region mapped by multimission satellite imagery. *Cryosphere* **8**, 977–989 (2014).
39. Mukherjee, K. et al. Surge-type glaciers in the Tien Shan (Central Asia). *Arct. Antarct. Alp. Res.* **49**, 147–171 (2017).
40. Vincent, C. & Moreau, L. Sliding velocity fluctuations and subglacial hydrology over the last two decades on Argentière glacier, Mont Blanc area. *J. Glaciol.* **62**, 805–815 (2016).
41. Nienow, P. W. et al. Hydrological controls on diurnal ice flow variability in valley glaciers. *J. Geophys. Res.* **110**, F04002 (2005).
42. Copland, L., Sharp, M. J., Nienow, P. & Bingham, R. G. The distribution of basal motion beneath a High Arctic polythermal glacier. *J. Glaciol.* **49**, 407–414 (2003).
43. Kääb, A. Combination of SRTM3 and repeat ASTER data for deriving alpine glacier flow velocities in the Bhutan Himalaya. *Remote Sens. Environ.* **94**, 463–474 (2005).
44. Schoof, C. The effect of cavitation on glacier sliding. *Proc. R. Soc. A* **461**, 609–627 (2005).

Acknowledgements

We thank M. Huss for providing the thickness and centre flow line data, J. Gardelle, T. Bolch, M. Rankl and H. Sevestre for providing data from their surge-inventory as well as glacier and basin outlines. We thank A. Rowan for comments and suggestions that greatly improved the quality of the paper. Initial research was conducted during A.D.'s graduate programme, with a doctoral fellowship from the Centre National d'Etude Spatial (CNES) and from the Savoie region. N.G. and A.D. were supported by funding from the European Space Agency Dragon 3 programme. E.B. acknowledges support from the French Space Agency (CNES). A.S.G. and A.D. were supported by funding from the NASA Cryosphere and MEaSUREs Programs and research was conducted at the Jet Propulsion Laboratory, California Institute of Technology, under contract with the National Aeronautics and Space Administration.

Author contributions

A.D., N.G. and A.S.G. designed the study. A.S.G. generated the velocity fields. A.D. conducted the analysis with A.S.G and N.G. providing input. A.D. developed the model with D.G. and P.W.N. providing input. F.B. provided the elevation change data. All authors interpreted the results. A.D. led the writing of the paper and all co-authors contributed to it.

Competing interests

The authors declare no competing interests.

Additional information

Supplementary information is available for this paper at https://doi.org/10.1038/s41561-018-0271-9.

Reprints and permissions information is available at www.nature.com/reprints.

Correspondence and requests for materials should be addressed to A.D.

Publisher's note: Springer Nature remains neutral with regard to jurisdictional claims in published maps and institutional affiliations.

Methods

Surface velocity. The JPL autonomous Repeat Image Feature Tracking (auto-RIFT version 0.9) processing scheme[23] was applied to all Landsat 4, 5, 7 and 8 Collection 1 LT1 images acquired over HMA between 1985 and 2017 with 60% cloud cover or less, as indicated in the image metadata. The images are pre-processed using a 5 by 5 Wallis operator to normalize for local variability in image radiance caused by shadows, topography and sun angle. For Landsat 4 and 5, along-track artefacts[45] are removed using Fourier filtering and a principal component analysis of bands 1 to 4 is used, whereas for Landsat 7 and 8 panchromatic (Band 8) images are used (15 m pixel size). Missing data in Landsat 7 images introduced after the Scan Line Corrector failure (SLC-off) are filled with random data so that they do not contribute to the amplitude of the correlation peak. Pre-processed image pairs were searched for matching features by finding local normalized cross correlation (NCC) maxima at sub-pixel resolution by oversampling the correlation surface by a factor of 16 using a Gaussian kernel and identifying the location of maximum correlation. The use of a Gaussian kernel greatly reduces the sensitivity of subpixel displacement estimates to 'pixel-locking'[46]. A sparse (1/4 of full search) NCC search is first used to determine areas of coherent correlation between image pairs. Results from the sparse search guide a dense search with search centres spaced such that there is no overlap between adjacent template windows. For HMA, image pixels located within a 2 km buffer of glacier surfaces were searched with a 240 m by 240 m search window. Image pixels located more than 2 km from a glacier were searched with a 480 m by 480 m search window, with areas of unsuccessful retrievals searched with a 960 m by 960 m window.

Image geometry between image pairs is highly stable, but images suffer from x and y geolocation errors of typically ~15 m. To correct for geolocation errors the component velocities are tied to stable surface wherein the median of each velocity component (V_x, V_y) is set to zero over the non-glacier surface. Velocity fields were also contaminated by match blunders (for example, matching along shadow edges or of surfaces obscured by cloud in one of the two images). Component velocities that deviate by more than three times the interquartile range from the median of all co-located pixels are assumed to be gross outliers and are removed. The uncertainty of each image-pair velocity field is set equal to the standard deviation in component velocities measured over stable surfaces.

Annual velocity maps are created by taking the error-weighted average of all image-pair velocity fields having a centre-date that falls within that calendar year. A mean velocity field ($\mathbf{V}_0$) is then created by taking the error weighted average of all annual velocity maps. The uncertainty of the merged velocities is estimated on a pixel basis by propagating the uncertainty of each measurement:

$$\sigma_X = \sqrt{\frac{\Sigma \sigma_{i,X}^2}{N}} \tag{3}$$

where X denotes the component x or y, σ_i is the uncertainty of each individual velocity field as estimated from the stable areas and N is the number of observations contributing to the weighted average. An effective date and pair time span are estimated for each pixel as a weighted average of the individual pairs' date and time span. Using this approach, we calculated yearly velocity maps from 1985 to 2017 that were derived from 2,287,223 unique image pairs (Landsat 4: 367, Landsat 5: 836,616, Landsat 7: 907,142, Landsat 8: 543,098). For our analysis, we excluded velocity estimates with large uncertainties —that is, where $\sigma = \sqrt{\sigma_x^2 + \sigma_y^2} > 5\,\mathrm{m\,yr^{-1}}$ and $N < 5$.

Velocity change. We estimate the velocity change compared to the mean velocity $\mathbf{V}_0$. We define the velocity anomaly as the value of the difference vector $\mathbf{V}_t - \mathbf{V}_0$ projected on the mean velocity vector:

$$\mathrm{dv} = \frac{(\mathbf{V}_t - \mathbf{V}_0)\cdot \mathbf{V}_0}{\|\mathbf{V}_0\|} = \frac{(V_{x,t} - V_{x,0})\,V_{x,0} + (V_{y,t} - V_{y,0})\,V_{y,0}}{\|\mathbf{V}_0\|} \tag{4}$$

The difference in velocity magnitude is typically used to characterize velocity change[7,22,47,48]. However, if each component of the velocity can be considered as following a symmetrical distribution, the distribution of the velocity magnitude, by definition, is skewed towards positive values with a non-zero mean. In the case of normally distributed noise, the velocity magnitude follows a Rice distribution that has a biased mean[49]. This bias decreases with the velocity magnitude and increases with the standard deviation of the velocity components (noise). A consequence of this bias is an apparent negative velocity trend in slow-moving areas when estimating changes between the earlier Landsat missions with a higher noise and the newer mission with a reduced noise (Supplementary Fig. 9). This bias affects velocity trends in areas where the velocity is not significantly larger than the noise. The proposed velocity anomaly has the advantage of having a noise that is symmetrically distributed around 0 that will not introduce a bias in the mean value (Supplementary Fig. 8), even for slow-moving areas.

Region of Interest. We restrict our analysis to the relatively fast moving part (mean velocity greater than 5 m yr^{-1}) of the ablation area of glaciers larger than 5 km^2. Glaciers smaller than several square kilometres tend to have velocities below our uncertainty threshold, few measurements, and narrow tongues of width similar to the correlation window, which highly decreases the confidence in these measurements. The ablation zone is approximated as all points located below the glacier median elevation $z < (z_{max} + z_{min})/2$, where z is the pixel elevation and z_{min} and z_{max} are the minimum and maximum altitude of the glacier to which the pixel belongs. z_{min} and z_{max} are extracted from the RGI 6.0 inventory[25] and z is extracted from the Shuttle Radar Topography Mission (SRTM) topography version 3[37]. These points are later referred as the Region of Interest (RoI).

Glaciers surges. We exclude glaciers with reported surge activity for parts of the analysis. We use inventories from previous studies[5,26,38,39] (Supplementary Section 4). We also exclude glaciers that were not identified as surging in those inventories but exhibit a behaviour typical of surge events (temporally and spatially limited speed-up, slowdown in an upper zone and acceleration at the tongue or reverse, thinning in an upper zone and thickening of the tongue or reverse). A list of surging glaciers are provided as Supplementary Data.

Velocity anomaly time series. To calculate the temporal evolution of the velocity anomaly for a given region, it is necessary to calculate statistics on pixels with observations for all years. However, as some years have lower spatial coverage, there is a compromise to be made between temporal and spatial coverage. The mask of common pixels is estimated as follows. The intersection of all valid pixels for all selected years is computed. If the coverage of the common mask is less than 25% of the RoI, the year with least coverage is excluded and the previous steps are repeated. As a result, years that do not meet the coverage criteria are excluded. Finally, for each region, the median and interquartile range of the velocity anomalies on the common mask are calculated. A trend in the regional velocity anomalies is calculated with uncertainty for the period 2000–2017 following the same methodology as below.

Velocity trends. We calculate a trend in velocity anomalies over the study period 2000–2016 for each 240 m by 240 m pixel of the annual velocity maps using a linear regression:

$$\mathrm{dv}(x,y) = a(x,y)t + b(x,y) \tag{5}$$

where dv is the velocity anomaly for the pixel located at position (x, y), t is the year of observation, and a and b are the parameters of the linear regression estimated at each pixel. To account for outliers, we perform the regression iteratively by removing observations with residuals larger than three standard deviations. The standard error σ_a (respectively σ_b) of the parameters a (respectively b) are estimated from the regression covariance matrix. We interpolate the velocity for year 2000 from the linear regression parameters:

$$V_{2000} = V_0 + a \times 2000 + b \tag{6}$$

and compute a velocity change relative to year 2000 (percentage change per decade) as:

$$\mathrm{ddv} = a \,/\, V_{2000} \times 10 \tag{7}$$

We estimate the uncertainty in the velocity trend using a Monte Carlo method by randomly drawing the first and last velocities of the study period from a Gaussian distribution determined from the regression uncertainty and then calculating the associated velocity change ddv. We repeat the operation 200 times and calculate the standard deviation of the distribution σ_{ddv}. Finally, we exclude all pixels with observations in less than 50% of years or $\sigma_{ddv} > 30\%$ decade^{-1}.

We generate the regional map of velocity trends by extracting the median, standard deviation $\sigma_{1°}$ and number of observations $N_{1°}$ of the velocity trend for 1° × 1° bounding boxes. The standard error is calculated as:

$$\epsilon_{1°} = \frac{\sigma_{1°}}{\sqrt{N_{1°}}} \tag{8}$$

Impact of the driving stress. Ice surface velocity is taken as

$$U_s = C\tau^m \tag{9}$$

where C and m are unknown parameters and τ is the driving stress (assumed equal to the basal stress), defined as

$$\tau(x) = \rho g H(x) \frac{\partial S}{\partial x}(x) \tag{10}$$

with ρ the ice density, g the gravitational acceleration, $H(x)$ the ice thickness and $S(x)$ the ice surface at the position x along a given flow line. In general, C and m are poorly constrained and likely to vary spatially. The only hypothesis we make in our analysis regarding these parameters is that they do not change over the time

interval of interest (2000–2016). A change in driving stress $\delta\tau$ hence induces a change in velocity according to:

$$U_s + \delta U_s = C(\tau + \delta\tau)^m \quad (11)$$

which can be rewritten as:

$$1 + \frac{\delta U_s}{U_s} = \left(1 + \frac{\delta\tau}{\tau}\right)^m \quad (12)$$

If our hypotheses are correct, a linear relationship is expected between $\log\left(1+\frac{\delta U_s}{U_s}\right)$ and $\log\left(1+\frac{\delta\tau}{\tau}\right)$ with a slope m.

Surface velocity is the sum, in various proportion, of basal sliding and ice deformation. By allowing for differing values of the exponent m, this model can encompass a range of sliding laws, such as those proposed for flow over hard beds with obstacles and without cavitation ($m=2$; ref. [33]); flow over deformable sediment ($m=1$; ref. [50]); or empirically derived laws from glacier observations ($m=3$; ref. [34]). Note that $m \leq 3$ for all of the above sliding laws; however, when subglacial pressure is high enough, cavitation (ice-bed decoupling in the lee of obstacles) is known to occur. Theoretical work suggests that basal drag is bounded independently of sliding velocity[44]. Heuristically we represent this as $m \gg 1$: it is not a physical model, yet it retains the quality that sliding with cavitation may be more sensitive to changes in driving stress than without.

Velocity due to ice deformation is represented as (ref. [32], section 8.3)

$$U_d = \frac{2Af}{n+1}\tau^n H \quad (13)$$

where A is the temperature-dependent creep parameter, f the valley shape factor and n the exponent of Glen's flow law[51]. For shear stresses taking place in a glacier, a value of $n=3$ is generally assumed (ref. [32] section 3.4.4). Assuming all parameters are constant with time, changes in driving stress $\delta\tau$ and thickness δH lead to

$$1 + \frac{\delta U_d}{U_d} = \left(1 + \frac{\delta\tau}{\tau}\right)^3 \left(1 + \frac{\delta H}{H}\right) \quad (14)$$

Considering that $\frac{\delta H}{H} \approx \frac{\delta\tau}{\tau}$ across all regions investigated (Supplementary Fig. 18, $R^2=0.97$), this can be rewritten as

$$1 + \frac{\delta U_d}{U_d} = \left(1 + \frac{\delta\tau}{\tau}\right)^4 \quad (15)$$

also compatible with our observations suggesting $m=4$. This relationship is also compatible with a contribution, in various proportions, of basal sliding and ice deformation to the surface velocity (Supplementary Section 5).

In practice, we compute the change in driving stress as follows:

(1) We extract ice thickness H_{2000} and elevation S_{2000} for year 2000 along centre flow lines at 50 m spacing (Supplementary Fig. 16a). The centre flow lines have been obtained using the method proposed by ref. [52] for each glacier of the Randolph Glacier Inventory (RGI) 5.0. We use ice thickness data provided by ref. [35]. The data have been validated with ground measurements and the 1-σ uncertainty estimated to 25%. These estimates might not well represent local variations in thickness but provide a good evaluation of a glacier's average thickness[36]. We use the Digital Elevation Model (DEM) from the C-band Shuttle Radar Topography Mission (SRTM-C) version 3 acquired in February 2000, available at 1 arc-sec (~30 m)[37].

(2) We use elevation change rates, obtained from a series of ASTER-derived DEMs for the period 2000–2016[3], to estimate the ice surface S_{2016} and thickness H_{2016} for year 2016. To account for gaps in the data and variability across the glacier, we calculate a mean elevation change for 50 m altitude bands at each glacier, instead of the centre line value, assuming that elevation changes are most strongly dependent on mean elevation. We calculate the uncertainty of the elevation trends for each altitude band using the same methodology as ref. [3].

(3) We calculate the surface slope $\left(\frac{\partial S_{2000}}{\partial x}\right)$ and $\left(\frac{\partial S_{2016}}{\partial x}\right)$ for both periods using a second-order central difference scheme.

(4) We calculate the driving stress along the flow line using equation (10) and apply a Gaussian filter of standard deviation $l=2H$ to account for the longitudinal coupling of the stress[53] (Supplementary Fig. 16b).

(5) We calculate a relative change in thickness $\left(\frac{\delta H}{H} = \frac{H_{2016}-H_{2000}}{H_{2000}}\right)$, driving stress $\left(\frac{\delta\tau}{\tau} = \frac{\tau_{2016}-\tau_{2000}}{\tau_{2000}}\right)$ and associated uncertainties for each point along the flow lines.

For comparison with the calculated driving stress, the trend in velocity anomalies is extracted along the centre flow lines at 50 m spacing. Points with uncertainty in the input parameters $\frac{\delta U_s}{U_s}$, $\frac{\delta\tau}{\tau}$ and $\frac{\delta H}{H}$ larger than 30% are excluded. Finally, a median value of all points within the RoI is calculated for each region for both the calculated driving stress and the observations.

Uncertainty. We use a Monte Carlo method to estimate the uncertainty due to the input parameters. We randomly draw (see below) H and δH to generate an ice surface and thickness. We calculate a thickness change and shear stress change profile and repeat the operation 200 times. We then compute the 68% confidence interval of the distribution in each point. H has an uncertainty of approximately 25%, and is positive. Therefore, H is multiplied by a factor drawn from a log-normal distribution with mean 1 and standard deviation 0.25. The random factor is drawn for each glacier individually, to account for the fact that errors in thickness are probably correlated for a single glacier due to the way ice thickness is modelled. δH is drawn from a Gaussian distribution whose mean and standard deviation are estimated from the distribution of values in the elevation band considered. As the δH values are drawn independently at each point, this can create step changes in the glacier profile, but, the smoothing used to account for the longitudinal stress coupling re-establishes a spatial correlation between neighbouring points. We calculate the regional uncertainty from each point's uncertainty σ_i as:

$$\sigma_{\text{reg}} = \frac{\sqrt{\sum \sigma_i}}{N_{\text{eff}}} \quad (16)$$

where N_{eff} is the number of independent points, calculated as the total number of points divided by 40. Here, we consider an average correlation length of 2 km as dictated by the smoothing (or an average thickness of 250 m), thus 40 points at 50 m spacing.

Data availability

The mean and annual velocity fields will be made publicly available in early 2019 as part of the NASA MEaSUREs - ITS_LIVE project and will be distributed though the National Snow and Ice Data centre. Data can be made available immediately through request to the authors.

References

45. Scherler, D., Leprince, S. & Strecker, M. R. Glacier-surface velocities in alpine terrain from optical satellite imagery—accuracy improvement and quality assessment. *Remote Sens. Environ.* **112**, 3806–3819 (2008).
46. Stein, A. N., Huertas, A. & Matthies, L. Attenuating stereo pixel-locking via affine window adaptation. In *Proc. IEEE International Conference on Robotics and Automation ICRA 2006* 914–921 (IEEE, 2006).
47. Tedstone, A. J. et al. Decadal slowdown of a land-terminating sector of the Greenland Ice Sheet despite warming. *Nature* **526**, 692–695 (2015).
48. Mouginot, J. & Rignot, E. Ice motion of the Patagonian Icefields of South America: 1984–2014. *Geophys. Res. Lett.* **42**, 1441–1449 (2015).
49. Gudbjartsson, H. & Patz, S. The Rician distribution of noisy MRI data. *Magn. Reson. Med.* **34**, 910–914 (1995).
50. MacAyeal, D. R. Large-scale ice flow over a viscous basal sediment: theory and application to Ice Stream B, Antarctica. *J. Geophys. Res.* **94**, 4071–4087 (1989).
51. Glen, J. W. The creep of polycrystalline ice. *Proc. R. Soc. A* **228**, 519–538 (1955).
52. Kienholz, C., Rich, J. L., Arendt, A. A. & Hock, R. A new method for deriving glacier centerlines applied to glaciers in Alaska and northwest Canada. *Cryosphere* **8**, 503–519 (2014).
53. Kamb, B. & Echelmeyer, K. A. Stress-gradient coupling in glacier flow: I. Longitudinal averaging of the influence of ice thickness and surface slope. *J. Glaciol.* **32**, 267–284 (1986).